

Dust Coma Morphology in the Deep Impact

Images of Comet 9P/Tempel 1

T. L. Farnham¹, D. D. Wellnitz¹, D. L. Hampton²,
J.-Y. Li¹, J. M. Sunshine¹, O. Groussin¹,
L. A. McFadden¹, C. J. Crockett¹, M. F. A'Hearn¹,
M. J. S. Belton³, P. Schultz⁴, C. M. Lisse⁵

¹ Department of Astronomy, University of Maryland, College Park, MD 20742

² Ball Aerospace and Technology Corp., Boulder, CO 80301

³ Belton Space Exploration Initiatives, Tucson, AZ 85716

⁴ Brown University, Providence RI 02412

⁵ Applied Physics Laboratory, Johns Hopkins University, Laurel, MD 20723

Abstract

We present an overview of the dust coma observations of comet Tempel 1 that were obtained during the approach and encounter phases of the Deep Impact mission. We use these observations to set constraints on the pre-impact activity of the comet and discuss some preliminary results. The temporal and spatial changes that were observed during approach reveal three distinct jets rotating with a 1.7-day periodicity. The brightest jet produces an arcuate feature that expands outward with a projected velocity of about 12 m s^{-1} , suggesting that the ambient dust coma is dominated by millimeter-sized dust grains. As the spatial resolution improves, more jets and fans are revealed. We use stereo pairs of high-resolution images to put some crude constraints on the source locations of some of the brightest features. We also present a number of interesting coma features that were observed, including surface jets detected at the limb of the nucleus when the exposed ice patches are passing over the horizon, and features that appear to be jets emanating from unilluminated sources near the negative pole. We also provide a list of 10 outbursts of various sizes that were observed in the near-continuous monitoring during the approach phase.

1 Introduction

Recent studies of comets suggest that most comet nuclei are essentially inactive, with fractional active areas typically measured to be a few percent (A'Hearn et al. 1995, Keller et al. 2004). Observations of jets, arcs and other features prompted suggestions that significant amounts of the activity in many comets were produced from isolated active areas or vents (e.g., Sekanina 1991, Keller et al. 2004 and references therein). Indeed, as ground-based observations have improved over the years, more and more comets have been observed to have coma features. Even comets that appear featureless at large distances reveal structure as they get close to the Earth, suggesting that, with enough resolution, features could be observed in the coma of any comet. In support of this conjecture, each of the four comets imaged by spacecraft (1P/Halley, 19P/Borrelly, 81P/Wild2 and 9P/Tempel 1) exhibited numerous well-defined, and even collimated, jets in their inner comae (e.g., Sagdeev et al. 1985, Sekanina and Larson, 1986, Soderblom et al. 2002, Brownlee et al. 2004, A'Hearn et al. 2005), including small-scale features that were not resolved in ground-based observations. The existence of these features in so many different objects suggests that there is a common mantling process (or other process that restricts local activity) that acts to insulate most of the comet's surface from sublimation. This mantle forms a protective covering that seals off the volatile material underneath. Only at breaks or thin spots in the mantle does activity persist to produce the coma. There are exceptions, including comet 46P/Wirtanen, where large fractions of the surface appear to be active (Farnham and Schleicher 1998, Groussin and Lamy 2003), which indicates that heavy mantling may not be a completely universal phenomenon. It is possible that other processes are acting to clear the mantle or to keep it from completely choking off the activity in the first place, but this appears to be less common than the mantling process itself. In any case, it has become clear that understanding the nature of the active areas is an important step in understanding the evolutionary processes that act on cometary nuclei.

Studies of the coma morphology and how it changes as a function of time provide information toward understanding the active areas. Dust features are particularly revealing because they tend to have a higher signal-to-noise than the gas features, and, because the dust maintains a relatively predictable trajectory after decoupling from the gas, the dust features represent a long-term record of emission that can be followed to large distances. The gas species provide an additional constraint on the activity but involve additional complications, including molecular dissociation that changes the composition of the outflowing material and leads to random excess velocities. When used in conjunction, however, studies of the gas and dust morphology can provide strong constraints on the nucleus activity. After the source regions have been identified, they can be studied to determine their physical properties and to investigate how they respond to the solar insolation that drives the comet's activity. Identification of the sources and characterization of their properties also provides constraints that can be used in other studies relating to seasonal effects, nongravitational forces, chemical inhomogeneities, or any other phenomenon relating to jet activity and the morphology of the dust or gas coma (Feaga et al. 2007, McFadden et al. 2006).

As the Deep Impact (DI) spacecraft approached comet Tempel 1 for its 4 July 2005 flyby and impact experiment, it obtained thousands of observations of the coma and nucleus. The temporal coverage was unprecedented, with images obtained every four hours for nearly two months before encounter. This sequence is invaluable for revealing the temporal changes in the coma and illustrating how details become clearer and more obvious as the spatial resolution improves. Early images showed a simple asymmetric coma with little structure, but as the

spacecraft closed on the comet, more and more features became apparent and were observed to change with time. Not only was the temporal coverage of the comet unprecedented, but the inner coma and nucleus were observed at a spatial resolution higher than ever before achieved. In the highest-resolution images, intricate structures are visible in the inner coma, at a level of detail never seen before. The asymmetries and features in the coma are most likely produced by active areas on the nucleus, which may consist of small, isolated spots or larger extended regions. The wealth of observations from the DI encounter presents us with an excellent means of exploring the connection between the coma and the active sources on the nucleus, to determine where the jets originate, to study the characteristics of the different sources, and to investigate the more general issue of mantling processes on the surface.

In this work, we present an overview of the DI dust coma observations that were obtained during the mission. We describe the morphology and how it changed throughout the approach and encounter with the nucleus and highlight some of the interesting features that were seen. We also present results from some preliminary measurements and outline the future analyses that will be done to bring the different aspects of the coma morphology into a broader general context.

2 Observations and Image Enhancements

The results presented here were derived from data obtained with the Medium Resolution Instrument (MRI) and the High Resolution Instrument (HRI) cameras aboard the DI flyby spacecraft and the Impactor Targeting System (ITS) camera on the impactor (Hampton et al. 2005). These images have a high dynamic range ($\sim 5 \times 10^3$) that allows bright nucleus features to be seen in the same frame in which coma features are visible off the limb. Occasional long exposures were also taken to improve the S/N of the coma. These long exposures tended to saturate the nucleus and inner coma, but they were typically obtained in conjunction with a shorter exposure that can be used to fill in for the saturated regions. For studies of the dust coma, we use the unfiltered images from the ITS and the MRI and HRI images obtained using the broadband context filters (~ 700 nm wide, centered at ~ 650 nm). Because these filters are broad, the observations are dominated by the sunlight reflected off the dust grains, producing high signal-to-noise images of the dust while minimizing the “contamination” from gas emissions. Basic processing of the images was done using the standard DI science pipeline, described by Klassen et al. (2007). It included bias removal using the CCD overscan regions, dark subtraction, flat fielding, corrections for frame transfer smear and conversion to absolute fluxes. Where appropriate, information about the specific observations is included with the individual discussions below.

Figure 1 shows an example of an MRI coma/nucleus image (left) and a high-resolution ITS image showing the detailed features on the nucleus (right). The coma image is formed from two separate frames: 9000852 is a 2 s exposure that captured the coma with a high signal while saturating the brighter nucleus; 9000848 is a 282 ms image obtained 30 seconds earlier that has a lower signal in the coma but unsaturated nucleus pixels. (The frame numbers are derived from the image sequences obtained by the different cameras, and provide a reference to the images that can be obtained from the Planetary Data System.) To account for the small difference in spacecraft range between the frames, the short exposure image was rescaled to match the spatial scale of the long exposure and then registered to the same position by aligning the radial jets visible in both frames. The two images were then combined by replacing the saturated and near-saturated pixels in the long exposure with the corresponding pixels from the short exposure. The

ITS nucleus image was created by inserting high-resolution images of the impact site into a lower-resolution image obtained earlier. The coordinate grid determined from the shape model was then overlaid.

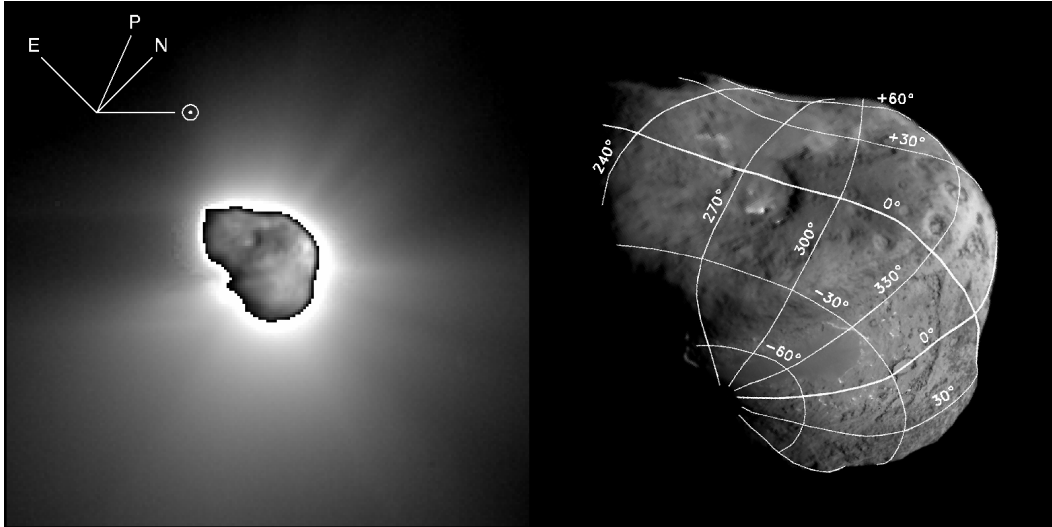


Figure 1. Example images of the coma and nucleus, showing coordinates used in the discussions. The left panel shows a composite MRI image, combining a long-exposure coma frame (9000852) with its corresponding short-exposure nucleus frame (9000848). The coma is displayed with a logarithmic scaling to show more structure, and the nucleus is inset with linear contrast levels, scaled so that it is not saturated. The spacecraft range was 1.4×10^4 km, and the field of view is about 28 km across. Celestial north and east, used to describe directions in the coma, are shown in the upper left, as are the projected positive spin axis (P) and sunward direction. The right panel shows a composite ITS image of the nucleus, produced by inserting higher-resolution images around the impact site into a lower-resolution image of the entire nucleus. The nucleus coordinate system, used for referencing features on the surface, is overlaid, with the positive pole to the upper right and longitudes increasing according to the right-hand rule as defined by IAU convention.

We are using observations from the different instruments to optimize the scientific results from our analysis. For the approach phase, the HRI images tend to be used because they provide a higher magnification of the coma, revealing features before they become visible in the MRI images. Unfortunately, a pre-launch calibration error resulted in the HRI camera being out of focus, which affects the resolution of the images (Klaasen et al. 2007). Although deconvolution procedures were developed to return the images to near their designed resolution (Lindler et al. 2007), these procedures work well only for very high signal-to-noise data because they amplify the background noise. For the lower S/N coma measurements, the deconvolution can introduce artifacts that would strongly affect, or even dominate, the coma features. Thus, we chose to use the out-of-focus HRI images for the following analyses, accepting that the resolution is degraded and adjusting our interpretations accordingly. (Ultimately, this has less of an effect for the coma than it would for the nucleus because the coma features tend to be broad and diffuse to start with, though any features narrower than the nine-pixel PSF will not be resolved.) Around the time when the nucleus is resolved, the spacecraft is close enough to the comet that the HRI

magnification is no longer an advantage, and for these times, MRI observations tend to be used to avoid the focus problems. The ITS is generally used in situations when high resolution is desirable or when a different viewpoint is required (e.g., for stereo visualization).

In general, most of the coma features tend to be radial with respect to the nucleus. Unfortunately, linear artifacts can result from different instrumental imperfections affecting the low-level signal in the image (<10 DN). Quadrant boundaries between the CCDs, incomplete removal of frame transfer smear and transient imperfections in the flat field corrections have the potential for leaving residuals along the rows and columns. In interpreting the features that are seen, it is important to account for these problems and to use different techniques to confirm that any features, especially those that are parallel to one of the CCD axes, are indeed real. For most of the approach images, the nucleus was purposely offset from the quadrant boundaries, minimizing the potential problems. Using multiple images in a sequence can also reveal transient flat-field problems, and during the encounter, when the most detail is observed, the ITS images can be compared to the MRI/HRI frames to aid in the interpretation of the features. The ITS image orientation is rotated about 30° relative to those of the MRI and HRI, and if a feature appears in both images, it is very likely to be inherent to the comet instead of an artifact relating to the instrument.

When studying the coma morphology, image enhancements are necessary to remove the bright central peak at the optocenter and to improve the contrast of the features. The choice of techniques is important because of the dramatic change in scales as the spacecraft closed from a distance of ~ 0.2 AU at the start of the data sequence on 7 May to 800 km when the flyby entered shield mode (800 s after impact). Although different techniques can certainly be used for different spatial scales, this introduces the possibility of multiple interpretations of the same feature at different times. Thus, a single technique is preferred, and after testing a number of different methods, we settled on a straightforward removal of a radial profile, with the same profile (described below) being used for all images. Division of a radial profile cleanly suppresses the bright central peak, while preserving the variations from that profile, in both the radial and azimuthal directions. We note that, regardless of the technique selected for most of the analysis, we routinely apply different enhancement routines to random images, including division by a ρ^{-1} profile, division by an azimuthal average and more invasive techniques such as unsharp masks and Laplace filters (Schleicher and Farnham 2004). The purpose of the multiple enhancements is to check for additional features that are not revealed by the selected technique and to evaluate whether artifacts are being introduced into the enhanced images.

For the Deep Impact data, we enhanced the images using a radial profile generated from the observations themselves, using a temporally and azimuthally averaged profile (Schleicher and Farnham 2004). First, a sub-sequence of images, consisting of 8–10 frames covering the 1.7-day rotation period, was selected. These frames were then adjusted to the same pixel scale and registered to a common center at the sub-pixel level. Combining this sub-sequence together produces a temporally averaged frame, where any variable coma features during a rotation have been smoothed out (in effect eliminating any arcs that would affect an azimuthal average). Finally, the temporally averaged image is averaged in the azimuthal direction to produce a single radial profile. This profile can be divided out of the individual frames to enhance the coma, revealing any deviations from this average profile. Because the spatial scale changes dramatically throughout the DI observations, several of these sub-sequences were used to produce radial profiles for different distances, which were merged into a single representational radial profile using the overlapping sections of the profiles to normalize them to the same scale.

The result is shown in Fig. 2 with six segments used to cover all available spatial scales. The innermost portion of each segment (within several point-spread functions) has been removed to avoid contamination from light reflected off the nucleus. Note that, because the scale is changing rapidly near close approach, the July segments are derived from single frames that have been azimuthally averaged, with no temporal averaging. This should pose no significant problems because the spacecraft is close enough to the nucleus that all features appear radial and thus, there are no arcs to significantly affect the azimuthal average (this assumption is supported by the lack of features in the July radial profiles). The composite curve that is created from the different segments is used to provide a uniform enhancement of the coma and can reliably be used from the most distant DI observations through the closest approach.

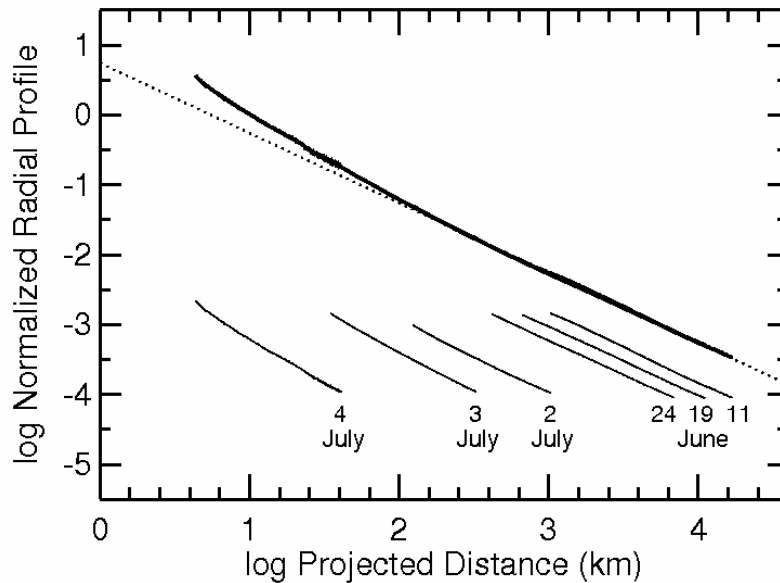


Figure 2. Azimuthally averaged radial profile of comet Tempel 1, created by combining coma measurements obtained at different distances during approach. Individual segments, shown at the bottom, are shifted vertically to align the overlapping regions. The dotted line represents a ρ^{-1} profile, which fits well to the coma regions outside ~ 300 km. Closer to the nucleus, the coma steepens, possibly indicating a zone of acceleration. See the text for additional discussion.

In addition to being useful as an enhancement tool, this result is scientifically interesting, as it represents the average radial profile of the coma. At large projected distances, the coma shows a canonical ρ^{-1} profile, which is consistent with a uniform outflow of the dust (averaged over a rotation). Within about 300 km, however, the profile steepens, indicating that the coma deviates in some way from uniform outflow. There are two basic scenarios that could explain this. First, the dust could be accelerating while it is entrained in the gas flow, which means that the gas and dust remain coupled out to a distance of a few hundred kilometers. Second, the steeper slope could be caused by physical changes in the dust particles or their scattering properties as they recede from the nucleus. Freshly ejected dust grains could be changing their albedo, shrinking (as icy components sublime away) or fragmenting, as was seen by Stardust at Wild 2 (Tuzzolino et al. 2004) or combinations of these changes. The fact that the radial profile beyond 300 km drops as the canonical ρ^{-1} indicates that there is no subsequent change in the dust beyond

that distance. The dust and gas have decoupled, stopping any acceleration of the grains, and/or the particles have stopped changing their physical properties.

3 Coma Morphology

The first Deep Impact images of comet Tempel 1 were obtained on 13 April, with occasional returns over the next few weeks. Intensive observations started on 7 May, when the spacecraft started to obtain images every four hours, though there are a few blocks of time when the monitoring was interrupted because of spacecraft problems, maneuvers or calibration measurements that preempted the comet observations. In the days closer to impact, the observational frequency was increased until it was essentially continuous around the time of encounter. The entire temporal sequence provides an invaluable tool for following both the short- and long-term activity and morphology of the coma.

In the following discussions, we refer to apparent directions in the coma with respect to the equatorial coordinate system on the plane of the sky. To avoid confusion when referring to directions relative to the nucleus, we adopt the IAU definition for coordinates on the nucleus, using positive and negative to refer to the poles and their corresponding hemispheres. These coordinate systems are shown in Fig. 1 for reference.

3.1 Approach Morphology

During the approach sequence, the flyby spacecraft range decreased almost linearly from 5.2×10^7 km on 7 May to ~ 800 km when the spacecraft entered shield mode after the impact event. Over this same time frame, the heliocentric distance of the comet decreased from 1.62 AU to 1.50 AU and the solar phase angle increased from 28° to 63° . Throughout the sequence, the viewing geometry remained nearly constant, with a shift in the viewpoint of less than 5° between the 7 May observations and the time the impactor was released (24 hours before impact) and only about 1° in the last month. This nearly constant geometry, combined with the spin axis derived from the shape model (with the positive pole oriented at RA= 294° , Dec= $+73^\circ$; A'Hearn et al. 2005, Thomas et al. 2007), indicates that the sub-spacecraft latitude remained at about -23° during the last month of approach, so the negative polar region is always visible. Thus, changes in the appearance of the coma do not come from variations in perspective, but instead must be due to temporal changes and/or improved spatial resolution. (The heliocentric distance changes by only 0.13 AU during this time, which is unlikely to produce significant changes in the activity.) Temporal changes can result from rotational modulation caused by the 1.7 day spin period (A'Hearn et al. 2005, Lisse et al. 2005) or inherent deviations in the comet's behavior as a function of time. After the flyby spacecraft executed its divert maneuver on 3 July (to change its trajectory so that its closest approach distance was 500 km), the viewing geometry changed more dramatically, with the spacecraft moving to more negative latitudes. (The sub-spacecraft latitude was at -26° at the time of impact and approached -50° before entering shield mode.) In addition, by that time, the spacecraft's motion had effectively overcome the rotation rate of the nucleus, so any coma changes seen during encounter are primarily due to the perspective shift, with less of a contribution from rotational variations.

From the earliest images, an asymmetry in the coma was evident (e.g., Fig. 1), with the surface brightness of a southern fan up to twice as bright as the darkest regions to the northeast. This asymmetry persisted through encounter. Asymmetries were also observed in H₂O and CO₂

measurements obtained just before impact (Feaga et al. 2007). Interestingly, the CO₂ structure more closely matches that of the dust than the H₂O, which tends to be concentrated in the sunward direction. This suggests that CO₂ is a significant contributor in driving the dust activity. As the spacecraft closed on the nucleus, individual features became distinguishable. In addition to the southern fan, a short radial spike became visible to the northwest. Neither the southern fan nor the northwest spike showed any variations with time in the early portions of the data sequence, but by mid-June, rotational variations were becoming detectable.

An example of the rotational changes is illustrated in Fig. 3, which shows a sequence of 11 HRI images spanning a single rotational phase (defined such that zero phase occurs at the time of impact). Each panel has been enhanced by dividing out the radial profile discussed in Section 2. We also note that a movie produced using images from June 13 through July 2 is available at www.astro.umd.edu/~farnham/Tempell/ and shows the changes in morphology that occur over many rotations. As shown in Fig. 3, the southern fan was resolved to be an arc-shaped feature, labeled “ α ,” that is produced by a jet, “A,” that oscillates in time with the rotation period. Soon thereafter, it was observed that the northwest jet was actually produced by two different sources, one of which becomes active about third of a rotation after the other (features “B” and “C”). These two linear jets must be near the same latitude on the positive hemisphere of the nucleus, as they produce the same morphology but with an offset in time. At a phase of about 0.2, jet “B” first becomes visible as a faint spike to the north. It rotates clockwise, brightening as it moves. Around phase 0.4, it lies to the northwest, where it stops rotating and then fades away. About a third of a rotation later, jet “C” repeats this same series of events.

The behavior of the “B” and “C” jets is easily explained if they both originate from the vicinity of about 30°-40° latitude in positive hemisphere and sweep out a cone as the comet rotates. A conceptual diagram illustrating this interpretation is shown in Fig. 4. Given the orientation of the nucleus, the cone lies with its closest edge near the plane of the sky, its farthest edge along the line of sight and directed away from the spacecraft, and its right edge pointing to the northwest. As a jet traces its path around the cone, it first enters sunlight when near the plane of the sky and pointing to the north. It initially moves westward in the plane of the sky, producing the apparent clockwise rotation, which slows as the jet’s cross-plane motion changes to into-the-plane motion at the right edge. When the jet points to the northwest, the apparent rotation stops, and the jet seems to fade away as it moves behind the nucleus. In this scenario, jet “C” must lie at a longitude about 120° lower than that of jet “B,” causing it to appear a third of a rotation later.

The southern jet is significantly more active than “B” or “C” and exhibits a more complicated morphology that can be followed for most of the rotation as it sweeps out its own cone around the negative pole (Fig. 4). At a phase of 0.75, a bright radial feature first appears toward the south (jet “A”). For about a third of a rotation, this feature rotates counterclockwise until it points southwest, at which time it reverses direction and moves clockwise again for another third of a rotation. This motion produces an arc-shaped feature (“ α ”) that expands outward from the nucleus with an edge to the southwest where the jet reverses direction. Although the arc can be seen moving outward, it rapidly spreads and diffuses, which is why it is not resolved from larger distances. Because the jet is always visible on one side of the nucleus, the spacecraft must lie outside of the cone, which restricts the location of the source to a latitude closer to the pole than the -23° sub-spacecraft point. An additional constraint on the location comes from the angle formed by the pole and the jet when the jet reverses its direction. This angle is consistent with a source that lies at a latitude around -45°, though the broad nature of the

jet suggests that it is probably an extended source rather than a small active vent (e.g., Samarasinha 2000, Schleicher and Woodney 2003). With this location, the near side of the cone is pointed roughly toward the spacecraft, and the far side is near the plane of the sky. Thus, the jet is highly projected as it moves from east to west across the visible side of the nucleus and then appears to change direction when it rotates around to the back side. For the return sweep, the jet is near the sky plane and is not as highly projected, producing a more well-defined arc.

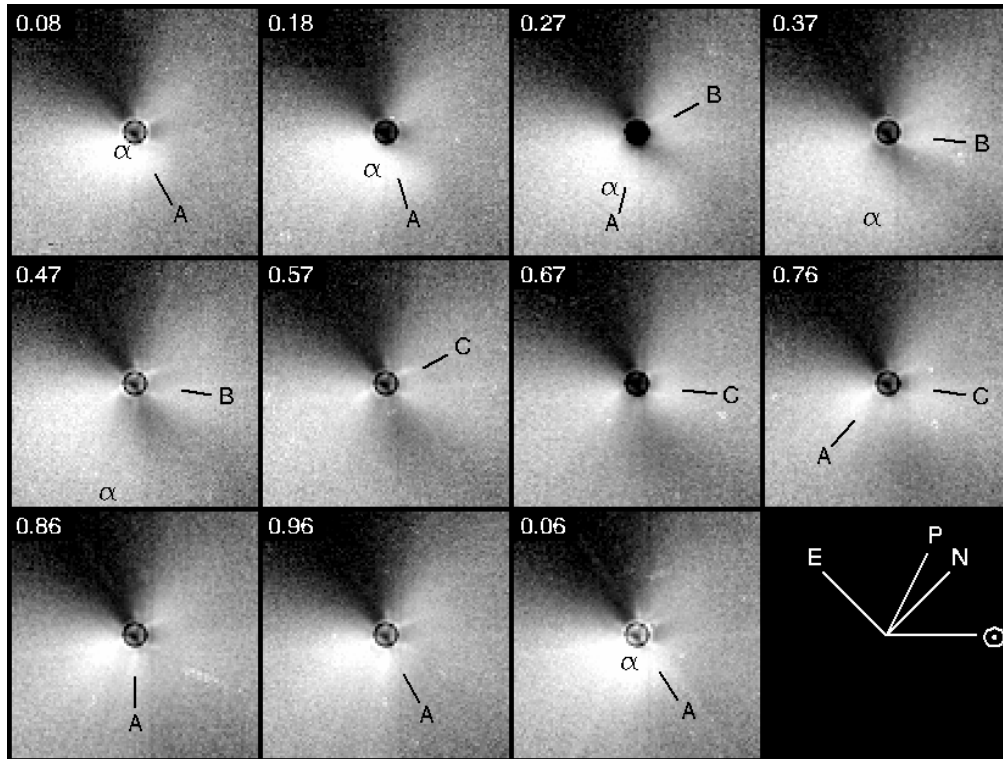


Figure 3. Sequence of HRI images from 27 and 28 June (frames 8000023 through 8200005) showing the coma morphology changes throughout a full rotation of the nucleus. The numbers in the upper left corner of each panel indicate the rotational phase at which each image was obtained (with zero phase defined by the time of impact). The three main jets, labeled “A,” “B” and “C,” and the arc structure labeled “ α ,” are discussed individually in the text. (Jet “A” defines the leading edge of the arc.) The lower right panel shows the orientation of celestial north and east as well as the direction of the Sun (which extends 30° out of the sky plane) and the rotation pole (which extends 23° into the sky plane). Images have been enhanced by removing an averaged radial profile as discussed in the text. The circle in the center covers the point spread function of the nucleus, which appears as a donut because of the HRI focus problem. The six-pointed “star” pattern, visible close to the nucleus, is produced by diffraction spikes and should not be interpreted as coma features. The field of view of the first frame is 1200 km and the last is 890 km, with an approximately linear change in between.

Using the coma morphology as a function of time and the orientation of the nucleus, we can investigate the status of the jet activity at the time of the encounter. Zero rotational phase is defined as the time of impact, so we are interested in the state of the coma features at that phase. Since jet “A” turns on at phase 0.75 and rotates westward until phase 0.1 (at which time it starts

to move back to the East), it will not only be active at the time of encounter, but it will be pointed in the general direction of the spacecraft. If the source is indeed at a latitude of -45° , then the jet axis will be offset from the line of sight by an angle of roughly 30° at the time of impact. Jet “B,” on the other hand, first becomes active around a phase 0.25 and is brightest between 0.4 and 0.5, so at zero phase, it will be pointed away from the Sun and will possibly be inactive. Similarly, jet “C” is first visible around phase 0.55 and peaks around 0.75. A quarter of a phase later, it may be shutting down, but even if it is still active, it will be on the opposite side of the nucleus pointing away from the spacecraft.

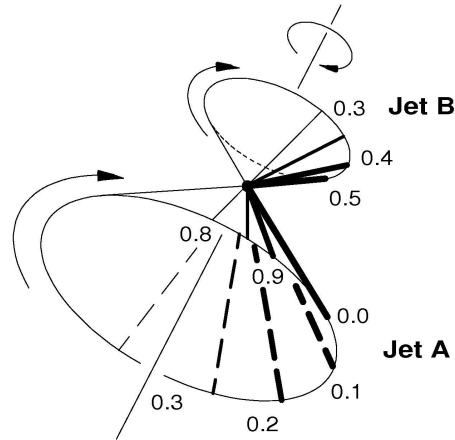


Figure 4. Conceptual diagram showing jets sweeping out cones as the nucleus rotates. The lower cone (with its opening toward the observer) is swept out by jet “A,” which is assumed to be at a latitude of -45° . The upper cone (with its opening pointing away from the observer) is swept out by jet “B,” assumed to be at a latitude of $+40^\circ$. (Jet “C” follows roughly the same cone as “B,” but is likely to be at a slightly lower latitude and is at a rotational phase 0.3 later.) Along the edges of each cone are labels to show the approximate direction of the jet at different rotational phases, corresponding to the panels in Fig. 3. The thickness of the lines along the walls of the cones represents the approximate activity level seen in that sequence, with solid lines on the side nearest the observer and dashed lines on the opposite side. Note that the material emitted from the jet is moving at a finite velocity and so will appear to spiral outward along the cone, producing a corkscrew morphology when seen from a distance.

The outward motion of arc “ α ” can be used to estimate the velocity of the dust grains that comprise it. Ambiguities arise because of the reversal of the jet’s motion, diffusion of the material as it moves, and projection effects, but using the center of the turnaround point for the distance measurement provides a reference that minimizes these issues. Over a 12 hour period, the center of the arc is observed to move outward a distance of about 500 km. This gives projected velocity of about 12 m s^{-1} , and even if the various ambiguities are taken into account, the velocities are likely to remain in the range of $10\text{--}15 \text{ m s}^{-1}$. This low velocity is consistent with preliminary models of ground-based data that concluded that the morphology of the southern fan must be the result of large, slow-moving grains. On the basis of the lack of long-term effects from radiation pressure, Samarasinha (private communication) suggests that the pre-impact dust emission is strongly dominated by large (\sim millimeter-sized) particles, with very few small grains. This is an interesting result when compared to the dust excavated in the impact, which is dominated by very small (\sim micron-sized) grains (A’Hearn et al. 2005, Schleicher et al.

2006). This indicates that there are variations across the nucleus, which could be due to inherent regional differences (Belton et al. 2007) or to evolutionary processes (e.g., mantle formation).

There is still much work to be done regarding these jets. Using detailed coma models to reproduce the temporal morphology, along with a rotating shape model of the nucleus, we will be able to determine much more accurately the locations of the jets, their angular extent on the surface, and the emission velocities of the dust grains. Thermal properties can also be constrained by studying how the activity turns on and off with the illumination conditions as the nucleus rotates (Groussin et al. 2007).

3.2 Approach photometry

The approach image sequence was also used for obtaining photometric measurements of the coma, to look for variations in the dust production rate as a function of time. To determine the coma brightness, photometry of the comet, including signal from both the nucleus and the inner coma, was measured from about 50 MRI images between 24 June and 3 July, using a square 5×5 pixel aperture centered on the optocenter. The signal from the nucleus was then computed, using the shape model described by Thomas et al. (2007), the 1.7-day rotation period (A’Hearn et al. 2005, Lisse et al. 2005) and the photometric properties of the surface derived by Li et al. (2007). Absolute brightness calibration of the nucleus came from the images obtained about one rotation before encounter, which were scaled to the disk-resolved photometry measured at the same phase at encounter. The synthetic nuclear lightcurve was then computed using the apparent cross section of the nucleus as it changes throughout the rotational phase and correcting for variations in the heliocentric distance and the spacecraft range. It is estimated that uncertainties in the photometric properties of the surface, rotational phase and solar phase angle correction (20%, 1% and 2%, respectively) produce errors in the lightcurve of a few percent. The computed nuclear signal was then subtracted from the measured brightness to leave the signal from the coma, which is shown in Fig. 5.

The coma lightcurve, spanning the 10 days before impact, shows a clear modulation with a period that is consistent with the 1.7-day period of the nucleus. Because the coma lightcurve is single peaked and there are no systematics with a period of 1.7 days, the lightcurve must be the result of variations in the dust production as the nucleus rotates. The rotational sequence in Fig. 3 reflects these brightness changes and shows that they are dominated by the southern jet. The signal-to-noise is much higher at the end of the sequence than at the start, which shows the increasing contrast between the on and off states of the jet as the spatial resolution improves. There is no clear evidence for variations produced by the “B” or “C” jets, partly because they are much weaker than jet “A” and partly because the contrast is damped out by having two jets at different longitudes.

3.3 Approach Outbursts

In addition to rotational variations, at least 10 spontaneous outbursts were captured between 7 May and 3 July, including three large ones (very bright ejecta extends over a large range of directions, visible for three or more images) and seven minor ones (fainter, smaller extent, visible for one or two frames). All of the events are detectable in both the HRI and MRI sequences, and some of them were observed in HST and ground-based studies. Table 1 contains a list of the outbursts, when they were first visible, and some general characteristics. (Note that

the actual onset of the outburst occurs before the listed time.) The larger outbursts were detected in the approach photometry and were discussed by A'Hearn et al. (2005), with the fainter ones subsequently found in the imaging data. The onset of these events appears to be impulsive, but several of the outbursts appear to maintain low-level activity that continues for up to several hours after the initial burst. In addition, the outbursts from 24 and 25 June, shown in Fig. 6, are clearly related, occurring about one rotation apart and exhibiting almost the exact same morphology.

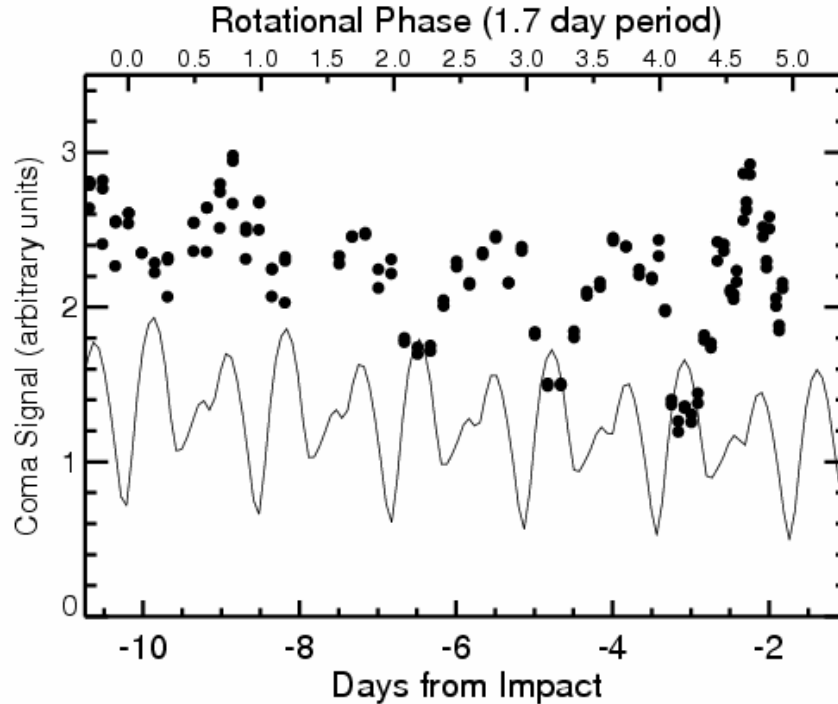


Figure 5. Photometric lightcurve of the coma of Tempel 1 during the DI approach. Single-peaked variations with a period of 1.7 days are clearly visible (dots). The variations correspond to the changes seen during the rotational phase in Fig. 3 and are dominated by the on/off cycle of jet “A.” The lightcurve was obtained by subtracting a model of the nucleus brightness (solid line) from aperture photometry measurements. The rotational phase axis is defined such that impact occurs at 6.0. Uncertainties are variable with time and can be estimated from the scatter in the measurements.

There is a strong concentration of events (7 out of 10) centered on a rotational phase of $0.95 (\pm 0.1)$, which suggests that there is a localized region on the surface that is more prone to outbursts than the rest of the nucleus. It is interesting that at this phase, the eastern facet, containing the exposed water ice patches (Sunshine et al. 2006), is just rotating into sunlight. The other three outbursts are also close in phase (0.35 ± 0.05), hinting that there might be a second region that is prone to occasional outbursts. We note that, even though the outbursts are clustered in phase, there is no strict periodicity between them, nor is there any consistency in strength, general appearance or direction of the ejecta. Furthermore, outbursts do not occur on every rotation, which means that they are not exclusively governed by rotational considerations. Thus, it is likely that the outbursts are produced from the same general region, but the specific sites are different in each case, and each one responds to the trigger mechanism in its own way. Currently, there is no evidence for any outburst activity at the time of the DI encounter. A

detailed analysis of these outbursts is underway to find their sources and to determine the physical processes that are driving them.

Table 1. Times and General Properties of Outbursts

UT Date	Time ¹	Rot. Phase ²	Size ³	Direction ⁴
May 30	05:19	0.37	Medium	NW — SE
June 03	09:19	0.83	Small	N — NW
June 13	21:19	0.05	Small	SW — S
June 14	13:19	0.40	Large	N — SE
June 18	17:19	0.85	Small	SE — S
June 22	21:19	0.30	Large	N — SE
June 24	01:19	0.00	Medium	S — SE
June 25	21:19	0.05	Medium	S — SE
June 30	17:52	0.95	Medium	SE — NE
July 02	08:50	0.90	Large	S — N

¹ Midtime of the image in which the outburst is first visible.

² Zero phase is defined as the time of impact.

³ Small outbursts are typically seen close to the nucleus in only one frame, Medium are seen at greater distances in one or two images and Large can be followed through several frames.

⁴ Apparent direction on the sky plane in equatorial reference frame. Range of directions is listed in the clockwise direction.

3.4 Encounter Morphology

During the encounter phase, images of the resolved nucleus were obtained with the MRI, HRI and ITS cameras. These images also captured the coma and revealed intricate details and numerous radial jets emanating from different regions on the surface. For studying the ambient coma, it is necessary to limit our data sample to pre-impact images because the ejecta curtain completely dominates the surface brightness of the coma after impact, masking the pre-existing features. There are exceptions, where small, bright features are seen very close to the surface, and these are discussed below. For the last images obtained before impact, the spatial scale was 89 and 18 m pix⁻¹ for MRI and HRI, respectively (both are frame 9000909 in their respective sequences). The last ITS image to show the entire nucleus (9000635) had a scale of 31 m pix⁻¹.

Although comparisons of the encounter images (with rotational phase 0.0) to those in the approach sequence of Fig. 3 are inevitable, they should be done with caution because the spatial scales are dramatically different. The entire field of view of the high-resolution images corresponds to less than two pixels in the frames shown in Fig. 3, introducing an offset in the apparent morphology that is dependent on the outward expansion speed of the dust. Furthermore, features look different at different resolutions. This is especially true regarding the southern jet, which is actually a segment of an Archimedean spiral, where outflowing material appears to be

radial when seen close to the nucleus but curves into arctuate structures when viewed from larger distances.

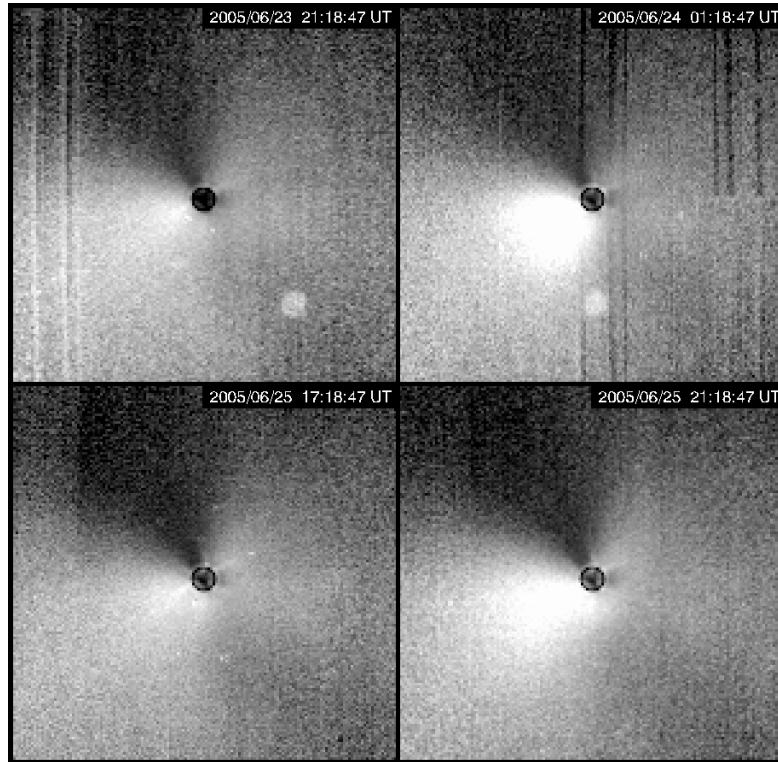


Figure 6. Outbursts from 24 and 25 June (HRI frames 6002351, 6002406, 6002533 and 6002542). For each pair of images, the panel on the right shows the first image in which the outburst is detected, while the panel on the left is the pre-outburst image obtained four hours earlier. The timing of these two outbursts, which were first detected in images obtained 44 hours apart, is consistent with them occurring at about the same phase on subsequent rotations. Furthermore, the morphology is nearly identical, which indicates that both outbursts probably originated from the same location. The field of view is about 1800 km in the top outburst and 1500 km in the bottom. The geometry is the same as that shown in Fig. 3.

Figure 7 contains the same coma image shown in Fig. 1, but it has been enhanced as described in Section 2 to improve the contrast of the jet features. Even after the nucleus is resolved, the coma exhibits the same basic morphology—bright to the south and dark to the northeast—that was observed during the approach, but a number of additional features have also become visible. (Most of the encounter images were obtained with shorter exposure times than were used for this image, and thus have lower S/N, but the main features still tend to be visible.) In Fig. 7, nine radial jets have been highlighted in red, with the edges of three broader fan structures outlined in yellow. An extension of the red lines across the face of the nucleus should pass over the source region of the jet unless the jet’s origin is on the far side of the nucleus.

To help determine whether a jet emanates from the near or far side of the nucleus, we can use parallax, produced either by the changing position of the flyby spacecraft as it passes the nucleus or by combining flyby images with ITS images. The resulting stereo information reveals whether the jet extends into or out of the plane of the sky. Figure 8 shows a stereo pair of images,

one from the MRI (9000909) and the other from the ITS (9000613), that had a separation of about 3° when the observations were obtained. These have been scaled to the same resolution and individually rotated (about 80° counterclockwise from the orientation in Fig. 7), so the spacecraft's motion is aligned from left to right. This orientation facilitates the stereo effect when viewed in cross-eyed format. Measurements were obtained of the centers of the more well-defined jets, and these are marked in the lower panels of the figure. These lines lead the eye in interpreting the perspective of the diffuse features, though the upper panels remain unmarked so they can be used to evaluate the result without interference. Using this preliminary analysis, we find that three of the brighter jets, 2, 3 and 4, all project out the plane of the sky and toward the spacecraft, while two of the jets, 6 and 7, point away from the spacecraft, indicating that their sources are probably hidden from view on the far side of the nucleus. Jets 1 and 5 lie roughly parallel to the motion of the spacecraft, so the stereo effect is not as prominent, but it appears that jet 1 also projects toward the spacecraft. Jets 8 and 9 are not visible in these images.

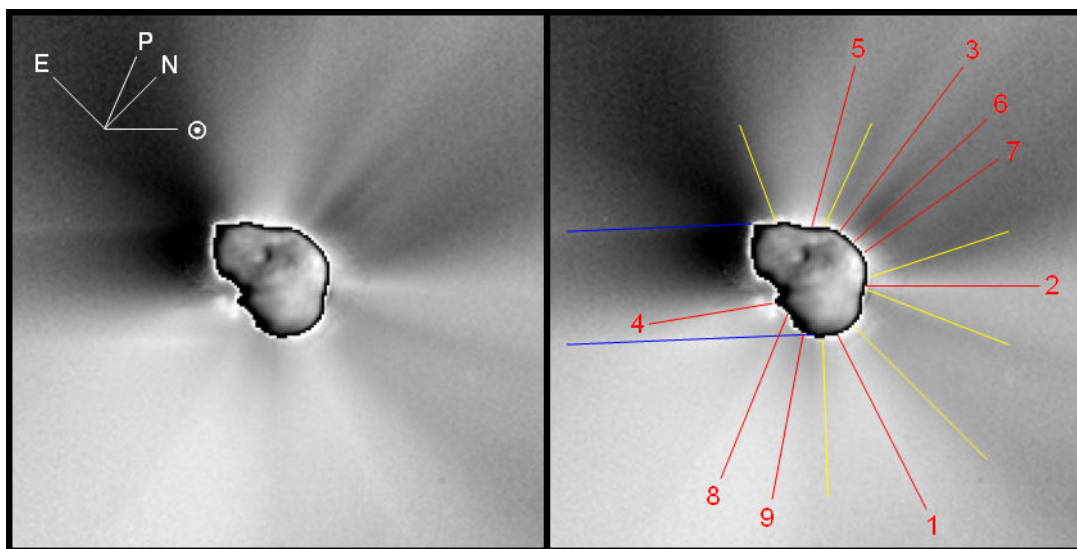


Figure 7. The coma image shown in Fig. 1, enhanced to improve the contrast of the features. The left panel shows the enhanced image, while the right panel shows the same image with radial jet features highlighted. Each red line denotes the bright centerline of a jet, while pairs of yellow lines define the “edges” of broader fan features. An extension of each line across the face of the nucleus should cross the jet’s source, though for clarity, this has not been done. (Also, some of the jets are likely to have their source on the far side of the nucleus.) The blue lines denote the edges of the shadow that is cast by the nucleus onto the coma. Linear displays are used for both the coma and the inset nucleus, but the ranges have been shifted by a factor of 10 so that both components can be seen in the same image. On the sunward side of the coma, the seam between the long-exposure coma image and the shorter-exposure nucleus image can be seen. See the caption for Fig. 1 for additional information.

Using the position angle of features on the sky, combined with the three-dimensional information from the stereo images, we can investigate the relationships between the jets and the nucleus. Jet 1, the brightest feature observed at encounter, matches well with the orientation and properties of jet “A,” the most prominent feature seen in the approach sequence. It is clear that these are the same feature, which originates from the western facet (the face where the impact

occurred). The orientation of the nucleus is such that the projection of the jet back to this facet necessarily intersects the surface at a latitude $-45^\circ \pm 15^\circ$ (compare the jets in Fig. 7 with the coordinates in Fig. 1), as was predicted in Section 3.1. The constraints from the temporal approach sequence, the stereo images and the high-resolution coma and nucleus images all suggest that this largest jet originates in the vicinity of the smooth patch at -45° latitude, 330° longitude. From this preliminary analysis, it is not clear whether the jet emanates from the surface of the patch itself or if the source is the edge of the patch or even the rougher surrounding terrain.

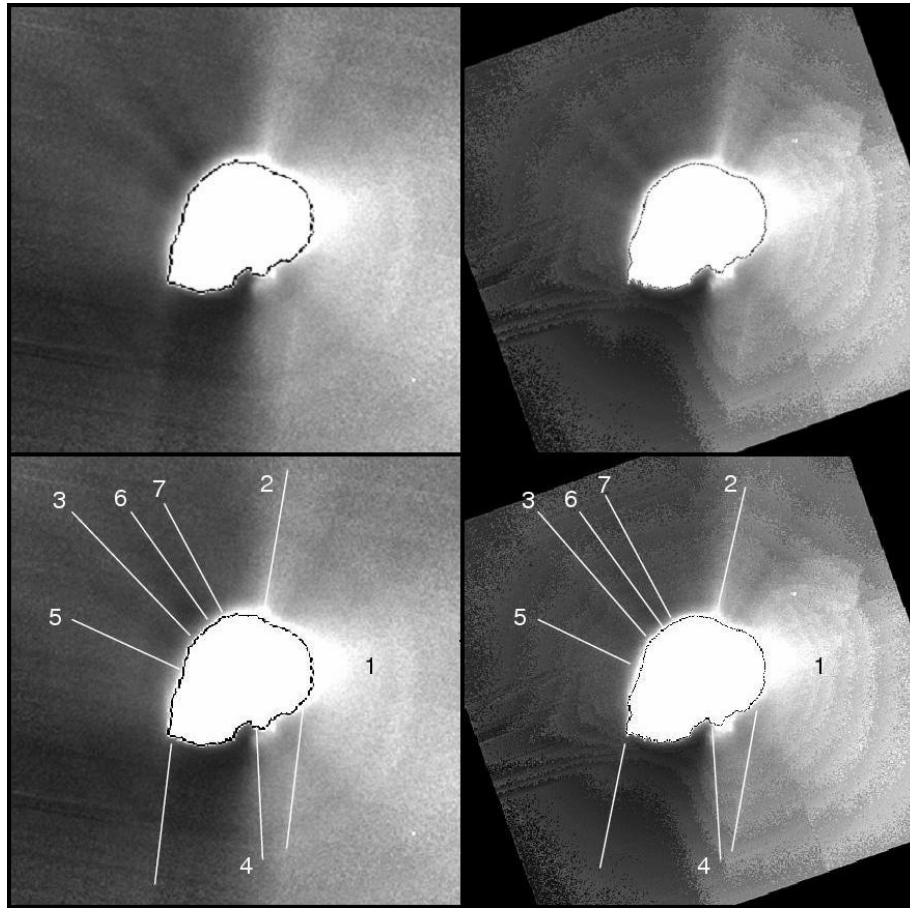


Figure 8. MRI (left) and ITS (right) images assembled as a stereo pair (viewed cross-eyed). The top and bottom pairs are the same, but the bottom set has the measured jet centers delineated with lines to aid the eye in interpreting the three-dimensional structure. Jets 2, 3 and 4 (which is part of a broad feature) project toward the observer, while 6 and 7 tilt away. Jet 5 shows little projection in or out, which may be due to the fact that it is nearly parallel to the spacecraft's motion, and therefore the parallax acts along the axis of the jet. The two unlabeled lines at the bottom are the edges of the nucleus' shadow. The quantization in the background levels of the ITS image are caused by the compression routines used to reduce the data transmission between the impactor and the flyby spacecraft. The orientation has been rotated 80° counterclockwise from that in Fig. 7 to put the spacecraft's motion along the horizontal direction.

None of the other features clearly correspond to jets “B” or “C” in the approach sequence. This is not surprising, as the properties of these jets are not well constrained at this rotational phase, either because they point away from the spacecraft or because they have turned off altogether. It is possible that the fan around jet 5 is associated with jet “B,” but the stereo imaging suggests otherwise. This fan seems to project out toward the spacecraft, and if this is the case, then it is at too high a longitude to reproduce the timing observed in the approach sequence. A more detailed future analysis will attempt to resolve this issue.

As for the other features, jet 2 appears to arise from a region near the equator in the vicinity of the sub-solar point. Terrain in this area is composed of pitted surfaces with close-packed (possibly erosional) depressions (Thomas et al. 2007). Features 3 and 5 are narrow, collimated jets (though a broad fan may be associated with jet 5). They both originate from the near side of the nucleus on the western facet and are discussed further in section 3.5. Jet 4 is relatively bright and probably provides a significant secondary contribution to the southward asymmetry. It appears to emanate from the polar region in the negative hemisphere and is discussed further in Section 3.6. Features 6 and 7 are narrow, highly collimated jets, with characteristics similar to those of features 3 and 5. The stereo images indicate that they originate on the far side of the nucleus and apparently have sources near the positive pole. The last two features, 8 and 9, are not well constrained, though they also seem to come from the region near the negative pole.

3.5 Surface Jets

Shortly before the flyby spacecraft entered shield mode, it obtained high-resolution images that show a number of small, well-defined jets whose bases are in contact with the nucleus. Four of these jets (denoted “a”–“d”) are shown in Fig. 9, which presents three representative frames from a sequence of 17 MRI images of the northern limb obtained over a period of 80 seconds. Chronologically, the images are reversed, with the third panel representing the earliest observation and the top panel showing the last image obtained of this limb. In the first panel, jet “a” is very faint and diffuse. In panel 2 it is brighter and more well-defined and then again fades and diffuses in panel 3. A movie showing this sequence is available at www.astro.umd.edu/~farnham/Tempell/. When it is at its brightest, it extends outward from the limb to a distance of about 500 m before fading into the background (which is brighter than normal because ejecta from the impact lie in the foreground). Feature “b” follows a similar pattern, though it does not get as bright or as sharp as “a.” Jets “c” and “d” are most clearly defined in the first panel (latest chronological time) and more diffuse in the others. The change in appearance and brightness of the jets is due to perspective changes produced by the spacecraft’s motion, which induced a shift of $\sim 30^\circ$ in the perceived position of the horizon during the sequence.

The orientation of surface jet “a” is roughly consistent with that of the more extended jet 3 in Fig. 7, though additional work needs to be done to confirm whether these are indeed the same feature seen at different scales. There is no obvious correlation of this type for jets “b,” “c” or “d,” but these are broader and more diffuse to start with. It is possible that “c” is associated with jet 5, or that emission from the surface jets simply merges together to produce (or at least contribute to) the broad fan structure to the northeast. Again, future work is needed to further evaluate these possibilities.

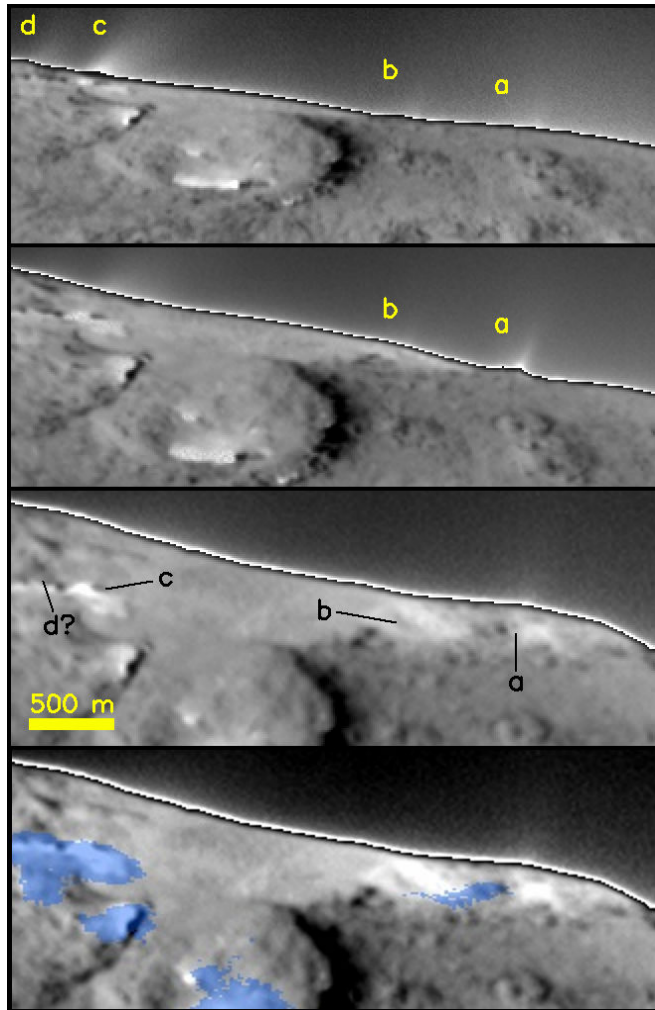


Figure 9. Sequence of representative MRI images (9001054, 9001042, 9001026) of the limb of the nucleus, showing at least four jets coming from the surface (“a”–“d”). The first three panels show the changing perspective of the horizon as the spacecraft moves underneath the nucleus (note that chronologically, the order of these panels is reversed). As the horizon shifts with time, the jets pass through the plane of the sky where they are highlighted and can be traced back to their source region on the surface. Each of the jets appears to emanate from a dark spot (designated by letters a–d in the third panel) adjacent to brighter material. In the fourth panel, regions where exposed water ice was detected are overlaid in blue for comparison. There seems to be a good correlation between the jet sources and the ice patches (see text for further discussion). The images are not enhanced, but the coma and nucleus are displayed at different contrast levels so that the nucleus does not saturate the display.

Because the jet is densest at its base, it appears brightest when its source is crossing the horizon (e.g., when the base is in front of or behind the limb, only the upper part of the column is visible above the horizon and the jet will appear fainter and more diffuse). Thus, we can use the position of the horizon when the jet is brightest to determine the location of the jet’s source to a fairly high degree of accuracy. Using this technique, we determined the approximate source for each of the four jets. We assumed that jet “c” was near its peak at the end of the sequence, because it was well defined and had a bright base that mimicked the appearance of jet “a” when

it was at its brightest. Source “d,” on the other hand, may or may not be near its peak, so its location is not well constrained. The locations we found are marked in the third panel of Fig. 9. Each of the four jets appears to come from a darker region on the surface, adjacent to a region of lighter material. (Lighter and darker are relative terms that fall between the surface albedo extremes of 3% and 6%.)

For comparison, the bottom panel in Fig. 9 shows the exposed ice patches that were observed on the surface (Sunshine et al. 2006). It is clear that the surface jets are associated in some way with the ice patches, as the jets appear when the ice is crossing the horizon and the source regions map back to sites that are adjacent to the ice. It is less clear what relationship exists between the two phenomena. On one hand, the patches could be the sources of the jets, while on the other hand, the jets could emanate from sub-surface vents, with a portion of the gas recondensing on the surface to produce the ice patches. The latter explanation is preferred because it provides a mechanism for replenishing the exposed ice, which should have a relatively short lifetime, given the thermal conditions on the surface (Groussin et al. 2007). The correlation between the jets and ice patches suggests that there may be additional surface jets emanating from the other patches, and they remain unseen simply because the limb was not imaged when those ice patches were on the horizon. Indeed, an extension of jet 5 across the nucleus does cross one of the ice patches (inside the large circular depression), raising the possibility of another connection that will be explored in future work.

3.6 Unilluminated Sources

Near the negative pole, there is another interesting phenomenon that may have important implications for long-term thermal lags that contribute to the activity on the nucleus. Figure 10 contains two different stretches of the same ITS image of the terminator near the comet’s negative pole. (The extension of jet 4 in Fig. 7 acts as a pointer to the region shown.) The left panel uses a typical display, showing the surface features near the smooth terrain at -45° . In the right panel, the display has been stretched by a factor of 10 (similar to stretches used to show other coma features). With the more extreme stretch, a series of coma features can be seen, highlighted against the darkened portion of the nucleus that lies beyond the terminator. These features appear to be jets of material that have risen above the local horizon into sunlight, where they are lit up and become visible against the dark background. Because they are completely disconnected from the sunlit areas of the surface, these jets seem to originate from sources that are not illuminated at the time of the observation. In fact, because the jets are so close to the negative pole (in the image, the cross marks the approximate pole derived from the shape model), many hours could have passed since the sources rotated into darkness. The longitudes of these jet features crossed the terminator around 10–15 hours before this observation, though topography is likely to change the actual amount of time that the sources have been in darkness. Stardust observed similar features, silhouetted against the dark portions of the nucleus of comet Wild 2, as well as radial jets extending beyond the limb that project back to the dark side of the nucleus (Sekanina et al. 2004).

The orientation of jet 4 (Fig. 7) may provide additional support for these features being active regions. Taking into account the general surface topography (from the shape model) and the fact that the jet points to the southeast, we conclude that the jet must have its source near the negative pole. Furthermore, as noted above, when jet 4 is projected back to the nucleus, it crosses directly over the unilluminated sources. Although there is not yet conclusive evidence

for a connection between the two features, these lines of evidence do raise the possibility that the unilluminated source is actually the point of origin of jet 4.

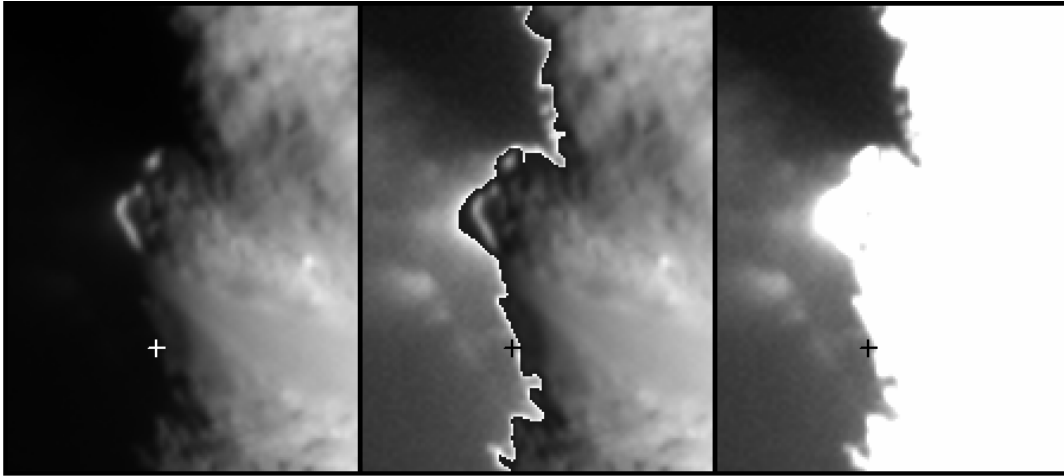


Figure 10. ITS image (9000642) showing the terminator of Tempel 1 with different display parameters. The left panel is stretched to show the illuminated portions of the surface. The stretch in the right panel is increased by a factor of 10 to show the region beyond the terminator, saturating the brighter illuminated regions but revealing coma features that appear to be coming from sources unilluminated by sunlight. The center panel combines the “optimally displayed” portions of each region to show the relative locations of the features. The cross in each panel marks the approximate location of the negative pole as determined from the shape model. The division above the cross is the morning terminator and below the cross is the evening terminator.

Work on these features is continuing, to confirm whether or not they are active regions, if they are indeed unilluminated, and to determine how much time has passed since they were last in sunlight. Additional work will be needed to confirm whether or not there is any connection to jet 4 or any other features in the coma. The results from this analysis may have important implications regarding the energy that drives cometary activity. Temperature measurements of the comet’s surface show that the thermal inertia is small, so there should be little thermal lag (Groussin et al. 2007). Thus, a source that remains active for even a few hours after illumination is cut off is evidence that there are additional factors that can modify the effects of the thermal inertia (e.g., seasonal effects can dominate over diurnal ones or sub-surface properties can differ from those at the surface). The low thermal inertia of the surface also suggests that the sub-surface layers experience relatively small temperature variations, and once activity has begun, it may continue well after the surface has passed into darkness. Another possibility is that the activity may be driven by ices that are volatile enough for sublimation to continue at the low temperatures present when the region is unilluminated. The work of Feaga et al. (2007) suggests that CO_2 could be a contributor.

4 Discussion

Deep Impact provided us with a wealth of data that can be used to study the coma of comet Tempel 1. In the preliminary analysis presented here, we have already found a number of interesting phenomena that require more detailed follow-up studies. We have taken the first

steps to determine the origins of some of the jets that were seen in the coma, but a significant amount of work remains. To more accurately determine the source locations of the jets, we will bring a number of tools into play, including an improved database of stereo image pairs that reveal the jet projections relative to the plane of the sky and use of the nucleus shape model (Thomas et al. 2007) to determine the point at which the jets intersect the surface. Once the sources have been found, we intend to explore the properties of those sites using the geologic maps of the surface, albedo maps, color maps, temperature maps, surface roughness, etc. We will also explore the behavior of the jets as a function of solar illumination using surface normals to gauge the level of activity at different solar incidence angles. The temporal approach sequence provides information that will be used to study the onset and cessation of activity as the sources (or at least jet “A”) rotate into and out of sunlight.

We will also use the results of our study of the spacecraft data to evaluate the techniques used in ground-based studies of cometary comae. Many jets are visible in the encounter images, yet only three are discernable in the approach sequence, and only the north/south asymmetry is visible in ground-based observations. This illustrates the point that distinct jets can blend together when observed at large distances or lower resolutions, so a feature observed in the coma can actually be the superposition of material emitted from multiple active areas. In the extreme case, all of the jets will blend together to produce a coma that appears featureless, even though there are many active areas on the surface. A number of important implications arise from this issue. The merging of features undoubtedly affects our ability to trace them from the outer coma back to their point of origin on the nucleus. The wide range of distances and resolutions available in the DI data set, along with the fact that the viewing geometry changed very slowly, provides an excellent opportunity for exploring the impact of this effect. As discussed in Sections 3.1 and 3.4, we were able to use the approach data to find the approximate location of jet “A,” indicating that the techniques are viable, at least to first order. However, from the encounter observations, we also know that other jets contribute to the southern asymmetry, even though they were not resolved in the early approach sequence. By comparing results from the early approach to those from late approach and encounter, we can evaluate how the derived source locations can be shifted by the superposition of the unresolved jets.

Another topic of interest is the relative coma contribution coming from isolated active areas versus that coming from broader extended sources. Even though only ~10% of the comet’s surface needs to be active to produce the observed production rates (A’Hearn et al. 1995), the scarcity of exposed water ice on the surface indicates that the majority of the gas production from Tempel 1 must come from sub-surface sources (Sunshine et al. 2006). Because of the presence of jets, we know that some fraction of the gas and dust is emitted from isolated vents, cracks or other gaps in a surface crust. However, it is also likely that there is a second contribution, where gas and dust percolate through a permeable mantle to produce a more uniform, background emission. We intend to explore the possibility of using the DI observations (along with ground-based observations) to separate the relative contributions from these components and to investigate how they act to produce the observed coma. These results will provide important constraints on the formation and evolution of mantles that act to regulate the comet’s activity levels.

Acknowledgements

We would like to thank the Deep Impact Science Team for useful discussions regarding the observations. This work was supported by NASA through contract NASW00004 from the Discovery Program to the University of Maryland. We also thank the referees Stephen Larson and Mihaly Horanyi for helpful comments.

References

- Ahearn, M. F., Hoban, S., Birch, P. V., Bowers, C., Martin, R., and Klinglesmith, D. A., 1986. Cyanogen jets in Comet Halley. *Nature* 324, 649-651.
- A'Hearn, M. F., Millis, R. L., Schleicher, D. G., Osip, D. J. and Birch, P. V., 1995. The ensemble properties of comets: Results from narrowband photometry of 85 comets, 1976-1992. *Icarus* 118, 223-270.
- A'Hearn, M. F., and 28 Coauthors, 2005. Deep Impact: Excavating Comet Tempel 1. *Science* 310, 258-264.
- Belton, M. J. S., Thomas, P., Veverka, J., Schultz, P., A'Hearn, M. F., Feaga, L., Farnham, T. L., Groussin, O., Li, J.-Y., Lisse, C., McFadden, L. M., Sunshine, J., Meech, K. J., Delamere, A., Kissel, J., 2007. The internal structure of Jupiter family cometary nuclei from Deep Impact observations: The Talps or "layered pile" model. *Icarus* (this issue).
- Brownlee, D. E., Horz, F., Newburn, R. L., Zolensky, M., Duxbury, T. C., Sandford, S., Sekanina, Z., Tsou, P., Hanner, M. S., Clark, B. C., Green, S. F., Kissel, J., 2004. Surface of young Jupiter family Comet 81P/Wild 2: View from the Stardust spacecraft. *Science* 304, 1764-1769.
- Farnham, T. L., Schleicher, D. G., 1998. Narrowband photometric results for Comet 46P/Wirtanen. *Astron. Astrophys.* 355, L50-L55.
- Feaga, L. M., A'Hearn, M. A., Sunshine, J. M., Groussin, O., Farnham, T., 2007. Tempel 1's H₂O and CO₂ inner coma asymmetries. *Icarus* (submitted).
- Groussin, O., Lamy, P., 2003. Activity on the surface of the nucleus of Comet 46P/Wirtanen *Astron. Astrophys.* 412, 879-891.
- Groussin, O., A'Hearn, M. F., Li, J.-Y., Thomas, P. C., Sunshine, J., Delamere, A., Lisse, C. M., Meech, K. J., Farnham, T. L., 2007. Surface temperature of the nucleus of Comet 9P/Tempel 1. *Icarus* (this issue).
- Hampton, D. L., Baer, J. W., Huisjen, M. A., Varner, C. C., Delamere, A., Wellnitz, D. D., A'Hearn, M. F., and Klaasen, K. P., 2005. An overview of the instrument suite for the Deep Impact mission. *Space Science Reviews* 117, 23-42.

- Keller, H. U., Britt, D., Buratti, B. J., Thomas, N., 2004. In situ observations of cometary nuclei. In: Festou, M., Keller, H. U. and Weaver, H. (eds.), *Comets II*. The University of Arizona Press, Tucson, pp. 211-222.
- Klassen, K. P., A'Hearn, M. F., Baca, M., Delamere, A., Desnoyer, M., Farnham, T. L., Groussin, O., Hampton, D., Ipatov, S., Li, J.-Y., Lisse, C. M., Mastrodemos, N., McLaughlin, S., Sunshine, J., Thomas, P., Wellnitz, D., 2007. Deep Impact instrument calibration. *Optical Engineering* (submitted).
- Li, J.-Y., A'Hearn, M.F., Belton, M. J. S., Crockett, C. J., Farnham, T. L., Lisse, C.M., McFadden, L.A., Meech, K.J., Sunshine, J.M., Thomas, P.C., Ververka, J., 2007. Deep Impact photometry of Comet 9P/Tempel 1. *Icarus* (this issue).
- Lindler, D., Busko, I., A'Hearn, M. F., White, R. L., 2007. Restoration of images of comet 9P/Tempel 1 taken with the Deep Impact high resolution imager. *PASP* (submitted).
- Lisse, C. M., A'Hearn, M. F., Groussin, O., Fernandez, Y. R., Belton, M. J. S., van Cleve, J. E., Charmandaris, V., Meech, K. J., McGleam, C., 2005. Rotationally resolved 8-35 micron Spitzer Space Telescope observations of the nucleus of Comet 9P/Tempel 1. *Astroph. J. Lett.* 625, L139-L142.
- McFadden, L.A., Crockett, C.J., Wellnitz, D.D., Feaga, L. M., A'Hearn, M.F., Farnham, T.L., Groussin, O., Li, J.Y., Lisse, C.M., Sunshine, J.M., Delamere, A., Klaasen, K.P., 2006. Gas and dust imaging of the inner coma of 9P/Tempel 1 before and after impact. *Bull. Am.Ast.Soc.* In press.
- Sagdeev, R. Z., Avanesov, G. A., Barinov, I.V., Debabov, A.I., Kvasikov, V. A., 1985. Comet Halley - Nucleus and jets (results of the VEGA mission). *Adv. Space Res.* 5, 95-104.
- Samarasinha, N. H., 2000. The coma morphology due to an extended active region and the implications for the spin state of Comet Hale-Bopp. *Astrophys. J. Lett.* 529, L107-L110.
- Schleicher, D. G., Woodney, L.M., 2003. Analyses of dust coma morphology of Comet Hyakutake (1996 B2) near perigee: outburst behavior, jet motion, source region locations, and nucleus pole orientation. *Icarus* 162, 190-213.
- Schleicher, D. G., Farnham, T. L., 2004. Photometry and imaging of the coma with narrowband filters. In: Festou, M., Keller, H. U. and Weaver, H. (eds.), *Comets II*. The University of Arizona Press, Tucson, pp. 449-469.
- Schleicher, D. G., Barnes, K. L., Baugh, N. F., 2006. photometry and imaging results for Comet 9P/Tempel 1 and Deep Impact: Gas production rates, postimpact lightcurves, and ejecta plume morphology. *Astron. J.* 131, 1130-1137.

- Sekanina, Z., Larson, S. M., 1986. Dust jets in Comet Halley observed by Giotto and from the ground. *Nature* 321, 357-361.
- Sekanina, Z. 1991. Cometary activity, discrete outgassing areas, and dust-jet formation. In: Newburn, R.L., Neugebauer and Rahe, J. (eds.) *Comets in the Post Halley Era*. Kluwer Academic Publishers, Boston, pp. 769-824.
- Sekanina, Z., Brownlee, D.E, Economou, T.E., Tuzzolino, A.J., Green, S.F., 2004. Modeling the nucleus and jets of Comet 82P/Wild 2 based on the Stardust encounter data. *Science* 304, 1769-1774.
- Soderblom, L. A., Becker, T. L., Bennett, G., Boice, D. C., Britt, D. T., Brown, R. H., Buratti, B. J., Isbell, C., Giese, B., Hare, T., Hicks, M. D., Howington-Kraus, E., Kirk, R. L., Lee, M., Nelson, R. M., Oberst, J., Owen, T. C., Rayman, M. D., Sandel, B. R., Stern, S. A., Thomas, N., Yelle, R. V., 2002. Observations of Comet 19P/Borrelly by the miniature integrated camera and spectrometer aboard Deep Space 1. *Science* 296, 1087-1091.
- Sunshine, J. M., A'Hearn, M.F., Groussin, O., Li, J.-Y., Belton, M.J.S., Delamere, W.A., Kissel, J., Klaasen, K.P., McFadden, L.A., Meech, K.J., Melosh, H.J., Schultz, P.H., Thomas, P.C., Veverka, J., Yoemans, D.K., Busko, I.C., Desnoyer, M., Farnham, T.L., Feaga, L.M., Hampton, D.L., Linder, D.J., Lisse, C.M., Wellnitz, D.D., 2006. Exposed water ice deposits on the surface of Comet 9P/Tempel 1. *Science* 311, 1453-1455.
- Thomas, P. C, Veverka, J., Belton, M. J. S., Hidy, A., A'Hearn, M. F., Farnham, T. L., Groussin, O., McFadden, L., Sunshine, J., Wellnitz, D., Lisse, C., Schultz, P., Meech, K. J., Delamere W. A., 2007. The shape, topography and geology of Tempel 1 from Deep Impact Observations, *Icarus* (this issue).
- Tuzzolino, A. J., Economou, T. E., Clark, B. C., Tsou, P., Brownlee, D. E., Green, S. F., McDonnell, J. A. M., McBride, N., Colwell, M. T. S. H., 2004. Dust measurements in the coma of Comet 81P/Wild 2 by the dust flux monitor instrument. *Science* 304, 1776-1780.